Modeling of the Evolution of the Microstructure and the Hardness Penetration Depth for a Hypoeutectoid Steel Processed by Grind-Hardening

Yu Guo [1]**, Minghe Liu** [2,*]**, Mingang Yin** [1] **and Yutao Yan** [1]

[1] School of Mechanical Engineering and Automation, Northeastern University, Shenyang 110819, China; guoyu@mail.neu.edu.cn (Y.G.); yinma@mail.neu.edu.cn (M.Y.); ytyan@mail.neu.edu.cn (Y.Y.)

[2] School of Mechanical Engineering, Shenyang Jianzhu University, Shenyang 110168, China

[*] Correspondence: rty26845@163.com; Tel./Fax: +86-24-2469-2186

check for
updates

Abstract: Grind-hardening processing is an emerging approach that combines the grinding and surface quenching process. During the process, the hardened layer—mainly martensite—is produced on the surface of the workpiece to achieve the purpose of surface strengthening. Above all, the surface temperature field of the hypoeutectoid-1045 steel workpiece was determined by finite element method for fully revealing the formation mechanism of the hardened layer. Further, the cellular automata approach was applied to dynamically simulate the transformation of both austenitization and martensitization from the initial microstructure. The hardness penetration depth was also predicted. Finally, a grind-hardening experiment was conducted to assess the theoretical study. Results showed that a combination of the finite element method and the cellular automata approach can effectively simulate the microstructure transformation of hardened layer. The microstructure and the hardness penetration depth were affected by the maximum grinding temperature and the heating rate. Research on the influence of grinding parameters showed that the hardness penetration depth increased as the depth of the wheel cut and feeding speed increased. Experiments revealed that the difference between predicted value and experimental value of the hardness penetration depth varied between 2.83% and 7.31%, which confirmed the effectiveness of the predicted model.

Keywords: grind-hardening process; cellular automata; microstructure evolution; prediction of hardness penetration depth

1. Introduction

Grind-hardening is an emerging technology for compound machining on the ground surface. This technology uses extremely high grinding heat generated during the grinding process to increase the surface temperature of the part to the austenitizing temperature in a short time. Then, the rapid cooling makes the surface experience martensitic transformation eventually, so as to achieve the purpose of surface strengthening [1,2]. The advantages of grind-hardening technology are obvious: (1) The effective combination of grinding and surface hardening simplifies the processing procedure, reduces energy consumption and improves productivity and economic benefits; (2) Compared with other grinding methods, grind-hardening technology cannot only make parts achieve higher machining accuracy, but also make the surface form a martensite microstructure, which significantly enhances its application performance in engineering (fatigue strength, wear resistance and corrosion resistance, etc.) [3]. Based on the above advantages, this technology has received continuous attention from scholars once it was proposed. Brinksmeire and Brockhoff et al. [4,5] carried out basic research on the grind-hardening process, using AISI 4140 steel and AISI E52100 steel as experimental materials, for revealing the factors

such as material properties, grinding parameters and wheel properties that influence on the formation of hardened layer. Foeckerer et al. established a 3D temperature field model for analyzing the influence of instantaneous grinding temperature distribution on the formation of hardness penetration depth (HPD) [6]. Alonso et al. predicted the HPD and proposed a method to optimize the surface roughness with the premise of ensuring the performance of the hardened layer by analyzing the change law of grinding specific energy [7]. Liu et al. conducted grind-hardening experiment on 41Cr4 steel and C45E4 steel to analyze the effects of material, wheel depth of cut, wheel speed and wheel characteristics on the depth and hardness of hardened layer [8]. Huang et al. established a prediction model for the residual stress of hardened layer based on the characteristics of the grinding force and verified it through grinding experiment [9]. From the above research, it can be seen that most scholars have conducted extensive studies on the formation mechanism and depth prediction of the hardened layer. However, the research mainly focuses on the effect of grinding heat on the part surface using finite element method (FEM) or the final microstructure analysis of the hardened layer by experiment using scanning electron microscope (SEM) and metallographic analysis. In fact, the excellent strengthening effect is mainly achieved by the hardened layer in grind-hardening process, whose formation is the result of a series of complex phase transformation in the surface microstructure with the action of the grinding heat. Based on the above considerations, analysis of the microstructure transformation process is the key to fully reveal the formation mechanism of the hardened layer and achieve effective prediction of its depth.

Currently, cellular automata (CA) is an effective approach for simulating the evolution of the microstructure for metallic materials. Using simple local rules and discretized space and time, this approach splits and merges complex systems and finally reproduces complex physical phenomena by simulating local effects simultaneously. The approach can also flexibly establish the transformation rules according to the metallurgical physical mechanism in the material phase transformation process so as to realize the dynamic evolution simulation of metal solidification, recrystallization and transformation [10–13]. Yang et al. established a CA model for the reaustenitization of hypoeutectoid steel and analyzed the grain size, austenite fraction and carbon concentration distribution of the microstructure of material after quenching process [14]. Aiming at the process of low-carbon steel ferrite–austenite transformation, An et al. established a 2D cellular automata model to comprehensively analyze the influence of austenite nucleation position, phase transformation driving force, thermodynamic parameters and carbon diffusion law on microstructure transformation [15]. Halder et al. conducted sensitivity analysis on the finite difference CA model of dual phase steels transformation in annealing process and revealed the influence law and extent of heat treatment parameters on microstructure transformation [16]. Su et al. established a 3D CA model of Fe–1C–1.5Cr alloy steel to simulate the grain growth process and analyzed the influence of different temperatures on the austenite grain growth [17]. From the above analysis, the current study for microstructure transformation applied CA approach has mainly focused on the heat treatment of metal materials, however there is a lack of relevant research on grinding process. Although the grind-hardening process can produce a martensitic microstructure on part surface, the difference between grind-hardening process and heat treatment is that the surface is not only subjected to the combined effect of grinding force and grinding heat, but also has no heat preservation similar to that of heat treatment. This causes the microstructure transformation of the hardened layer to be different from previous related studies in materials science. To sum up, considering the characteristics of the grind-hardening process, the application of CA approach to simulate the microstructure transformation process of the hardened layer will contribute to reveal the formation mechanism of the hardened layer and reduce the prediction difference of HPD.

Taking hypoeutectoid-1045 steel as the research object, this paper advances a coupled mathematical model of grinding force and grinding heat to simulate the instantaneous change and distribution of the surface temperature field during the grind-hardening process. On this basis, the transformation process of the initial microstructure to austenite and then to martensite is simulated dynamically and

visually for revealing the formation mechanism of the hardened layer and predicting HPD. The issue has important engineering significance for perfecting the theory and accelerating the development of grind-hardening technology.

2. Materials and Methods

2.1. Heat Source Model for Grind-Hardening Process

During the grind-hardening process, the cutting of the surface of the workpiece by the wheel abrasives converts most of the grinding mechanical energy into heat energy. Due to the heat conduction effect, the grinding heat will mainly diffuse to the wheel, workpiece and chips, as shown in Figure 1.
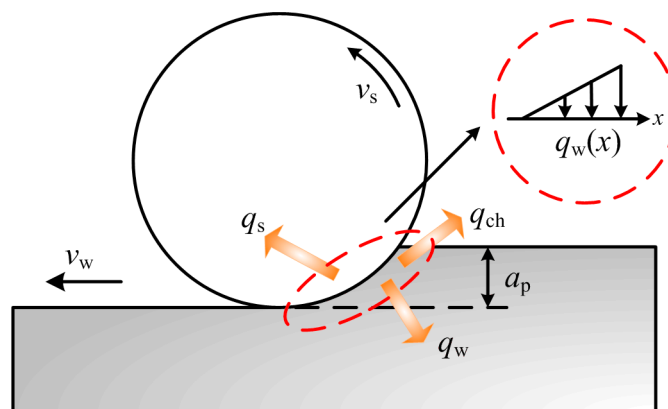
Figure 1. Grinding heat source and boundary conditions.

The total heat flux q_t generated by the grinding force is given by:

$$q_t = q_w + q_s + q_{ch} \tag{1}$$

where, q_w, q_s and q_{ch} are the heat conducted by workpiece, the wheel and the chips, respectively.

The heat flux conducted to the workpiece can be expressed as [18]:

$$q_w = R_w \frac{F_t(v_s \pm v_w)}{bl_c} \tag{2}$$

where, F_t is tangential grinding force; v_s is wheel speed; v_w is feeding speed; $v_s \pm v_w$ is related to the grinding modes; b is grinding width; l_c is length of grinding arc and $l_c = \sqrt{a_p \cdot d_s}$. a_p is wheel depth of cut and d_s is wheel diameter. The proportional coefficient of the heat transferred to the workpiece R_w can be expressed as:

$$R_w = \frac{1}{\sqrt{1 + \frac{(\lambda \rho C)_s}{(\lambda \rho C)_w}}} \tag{3}$$

where, $(\lambda \rho C)_s$ and $(\lambda \rho C)_w$ are the heat parameters of the wheel and the workpiece; λ is heat conductivity; ρ is material density; C is heat capacity.

Since the arc of contact between the wheel and the workpiece is close to a straight line, it can be considered that the distribution of the heat source is approximately triangular. Therefore, in the finite element simulation of the grinding temperature field, the heat source distribution adopts the triangular heat source model, as shown in Figure 1. The model can be expressed as:

$$q_w(x) = \frac{2q_w x}{l_c} \quad 0 \le x \le l_c \tag{4}$$

2.2. Dynamic Model for Microstructure Transformation Based on CA

Hypoeutectoid steel is a kind of structural steel with a carbon content 0.02 wt%~0.77 wt%. The initial microstructure is mainly composed of ferrite and pearlite. It can be known from the foregoing that the microstructure of hardened layer is dominated by martensite. The formation of martensite mainly goes through two stages. (1) Austenitization of the initial microstructure, namely $\alpha + P \rightarrow \gamma$, where α represents ferrite, P represents pearlite, and γ represents austenite. In this stage, the realization of austenitization requires three processes, namely nucleation, grain growth and coarsening; (2) As the austenite is cooled, a non-diffusion transformation appears on the surface to form martensite. Consequently, dynamic models for microstructure transformation in two stages illustrated above is contributed to simulate the microstructure evolution of hardened layer.

2.2.1. Determination of Austenitization Starting Temperature

For hypoeutectoid steel, once the surface of the workpiece is heated to austenitization starting temperature (Ac_1) or above, the pearlite starts to transform into austenite first. As the temperature continues to rise, ferrite will gradually transform into austenite. When the temperature goes above Ac_3, transformation finishes, and the surface is full of austenite [19]. Ac_1 is a function which is related to heating rate, initial microstructure and material composition. Moreover, Ac_1 is the starting temperature for the transformation from pearlite to austenite, which affects the driving force of phase transformation related to the nucleation of austenite and grain growth. In grind-hardening process, due to the effect of heat conduction, the heating rates varies from different position-to-position along the grinding depth of the workpiece, which in turn causes Ac_1 to be different. On this consequence, accurate evaluation of Ac_1 will not only affect the entire austenite transformation process, but also affect the prediction of HPD.

Based on Orlich's curves for hypoeutectoid-1045 steel, Ac_1 can be expressed as [20]:

$$Ac_1 = \begin{cases} 4.8421 \log^3(\varphi) + 3.3313 \log^2(\varphi) + 8.234 \log(\varphi) + 735.91, & \varphi < 150\,°C \\ 790, & \varphi > 150\,°C \end{cases} \tag{5}$$

where, φ is the heating rate, which can be obtained by grind-hardening temperature field simulation or experiment.

2.2.2. Dynamic Model for Austenite Transformation

When the temperature exceeds Ac_1 during heating, the austenite nuclei may appear both in the pearlite and at ferrite–pearlite interface (α/P interface) continuously. Simultaneously, nucleation process occurs continuously as the grinding temperature rises and ends until entire pearlite transforms into austenite. The probability of nucleation at α/P interface is generally considered greater than that in the pearlite because of the different energy effect [21]. The nucleation process with CA is shown in Figure 2.

(a)   (b)
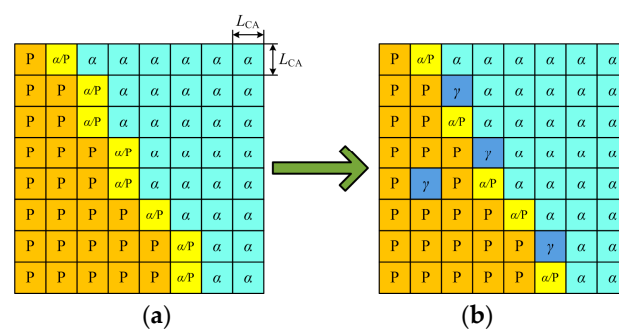
Figure 2. Schematic diagram of nucleation in cell lattice. (**a**) Before nucleation; (**b**) after nucleation. α represents ferrite, P represents pearlite, γ represents austenite and α/P represents ferrite–pearlite interface.

From literature [22], the nucleation rate can be expressed as:

$$\dot{n} = \alpha \times \varphi \times N_d \times f_P \times A \tag{6}$$

where, α is a factor, which depends on the mean interlamellar spacing in pearlite; f_P is the fraction of pearlite in the calculation domain; A is the area of entire computational domain or subdomain; N_d is the nucleation density, which can be expressed as:

$$N_d = f_N \exp\left(-\frac{Q_N}{k\left(T - T_{Ac_1}\right)}\right) \tag{7}$$

where, k is Boltzmann's constant; f_N is influence factor on nucleation structure of pearlite; Q_N is activation energy of austenite nucleation; T is the instantaneous grinding temperature at a certain moment.

Coupling Equations (6) and (7), the nucleation probability can be expressed as:

$$P = \dot{n} \times \Delta t \times S_{CA} \tag{8}$$

where, Δt is the time corresponding to each step in simulating; S_{CA} is cell area per unit, which is calculated by $S_{CA} = L_{CA}^2$, L_{CA} is the side length of the cell, as shown in Figure 2.

Once the austenite nucleation starts, the austenite grains begin to grow as well. The grain growth process can be described as both the transformation of pearlite to austenite and the transformation of ferrite to austenite. Due to the short diffusion distance in pearlite, the effect of carbon diffusion on the grain growth of austenite in pearlite is always ignored. Hence, pearlite can be considered to be directly transformed into austenite [23]. The transformation velocity of pearlite to austenite is given by:

$$v^{\gamma/P} = f_G \exp\left(-\frac{Q_G}{k\left(T - T_{Ac_1}\right)}\right) \tag{9}$$

where, f_G is the influence factor of pearlite on growth rate; Q_G is activation energy of growth.

Unlike the pearlite transformation, the ferrite transformation process is assumed to be a carbon diffusion-controlled and interface-controlled transformation. Actually, the carbon diffusion process starts together with the nucleation of austenite on the initial microstructure and accompanies by the entire grain growth process. The growth process of austenite grains is manifested by the migration of grain boundaries, but in essence, it is the changes in the chemical driving force caused by the diffusion of carbon atoms between ferrite and austenite. According to the 2nd Fick's law, the governing equation of carbon atom diffusion is given by [24]:

$$\frac{\partial C_E}{\partial t} = D_E\left[\frac{\partial^2 C_E}{\partial x^2} + \frac{\partial^2 C_E}{\partial y^2}\right] \tag{10}$$

where, C_E is equivalent concentration; D_E is diffusion coefficient in the α/γ interface cell, which varies with temperature; t is time.

The growth velocity of the γ/α interface is given by:

$$v^{\gamma/\alpha} = M^{\gamma/\alpha} \Delta G_{\alpha \to \gamma} \tag{11}$$

where, $M^{\gamma/\alpha}$ is grain boundary mobility of γ/α; $\Delta G_{\alpha \to \gamma}$ is the chemical driving force for interface motion. $M^{\gamma/\alpha}$ is calculated by:

$$M^{\gamma/\alpha} = M_0^{\gamma/\alpha} \exp\left(-\frac{Q^{\gamma/\alpha}}{RT}\right) \tag{12}$$

where, $M_0^{\gamma/\alpha}$ is the pre-experimental factor; $Q^{\gamma/\alpha}$ is the activation energy for boundary migration; R is the gas constant; T is absolute temperature.

$\Delta G_{\alpha \to \gamma}$ is calculated by [25]:

$$
\begin{aligned}
\Delta G_{\alpha \to \gamma} = {} & 3RT \ln(1 - y_{c\alpha}) - RT\left(1 - y_{c\gamma}\right) + y_{c\gamma}^2 (21058 + 11.58T) + 3.31(T - 1000) \\
& - 0.0983(T - 1000)^{0.96} + 7.11 \sin(0.034(T - 1000)) - 338.1
\end{aligned}
\tag{13}
$$

where, $y_{c\alpha}$ and $y_{c\gamma}$ are the molar fractions of carbon atoms in ferrite and austenite, respectively, that is given by $y_{c\alpha} = \frac{x_c}{3(1-x_c)}$ and $y_{c\gamma} = \frac{x_c}{1-x_c}$. x_c is molar fractions of carbon atom for the material.

As the austenite grains grows up continuously, austenite with different grain orientations come into contact. Meanwhile, their grain boundaries will move to the center of curvature in the driving force action of grain boundary migration and eventually cause austenite grains coarsening [23,26]. The velocity of the grain boundary segment, which describe the grain coarsening process, can be expressed by:

$$
v^{\gamma/\gamma} = M^{\gamma/\gamma} P
\tag{14}
$$

where, $M^{\gamma/\gamma}$ is the boundary mobility between austenite grains, that is given by:

$$
M^{\gamma/\gamma} = M_0^{\gamma/\gamma} \exp\left(-\frac{E^{\gamma/\gamma}}{RT}\right)
\tag{15}
$$

where, $M_0^{\gamma/\gamma}$ is the pre-experimental factor; $E^{\gamma/\gamma}$ is the activation energy for grain boundary migration.

The driving force of grain boundary migration P can be expressed as:

$$
P = \gamma_i \kappa
\tag{16}
$$

where, γ_i is the austenite grain boundary energy. According to Read–Shockley equation, γ_i is given by:

$$
\gamma_i =
\begin{cases}
\gamma_m & \theta_i \geq 15° \\
\gamma_m \frac{\theta_i}{\theta_m}\left(1 - \ln\frac{\theta_i}{\theta_m}\right) & \theta_i < 15°
\end{cases}
\tag{17}
$$

where, θ_i is orientation difference between adjacent austenite grains; θ_m is the orientation difference with the large crystallographic angle. In this study, $\theta_m = 15°$. γ_m is interface energy with the large crystallographic angle.

κ is the curvature of the austenite grain boundary that is given by:

$$
\kappa = \frac{1}{r_i} - \frac{1}{r_j}
\tag{18}
$$

where, r_i and r_j are the principle radii of the grain boundary segment of the two grains in contact.

2.2.3. Dynamics Model of Martensitic Transformation

The Martensitic transformation is a non-diffusion transformation. According to the theory of metal phase transformation, the driving force required for martensite formation $\Delta G^{\gamma-M}$ is given by:

$$
\Delta G^{\gamma-M} = \Delta G^{\gamma-\alpha} + \Delta G^{\alpha-M}
\tag{19}
$$

where, $\Delta G^{\gamma-\alpha}$ is increased value of free energy when the austenite is transformed into ferrite; $\Delta G^{\alpha-M}$ is increased value of free energy when the ferrite transformed to martensite. The martensitic transformation will take place only when the material temperature is lower than the martensitic transformation starting temperature Ms and $\Delta G^{\gamma-M} < 0$ simultaneously. In other words, Ms is a key factor affecting the martensite transformation. Ms can be defined as the temperature of the material

when $\Delta G^{\gamma - M} = 0$, namely $-\Delta G^{\gamma - \alpha} = \Delta G^{\alpha - M}$. For Fe–C alloys, the Ms is closely related to the chemical composition of the steel. Therefore, Ms can be calculated by [27]:

$$Ms = 539 - 423C - 30.4Mn - 17.1Ni - 12.1Cr - 7.5Mo \tag{20}$$

It can be seen from the foregoing that the hardened layer is formed by martensitic transformation in continuously cooling conditions. Hence, this formation belongs to athermal martensite transformation, whose amount of change only depends on the termination temperature by cooling but has nothing to do with the time spent at that temperature. The relationship between martensite transformation and cooling temperature can be expressed as [28]:

$$f = 1 - \exp\left[\alpha\left(Ms - T_q\right)\right] \tag{21}$$

where, f is the fraction of martensite; T_q is termination temperature of transformation; α is a constant and $\alpha = -0.011$ is taken for Fe–C steel with carbon content less than 1.1%.

3. Results and Discussions

3.1. Temperature Field Simulation and Discussion of Hardened Layer

Basing on the heating source model, the temperature field of 1045 steel workpiece during the grinding process is simulated by FEM. The material parameters of 1045 steel are shown in Table 1. The grinding temperature field is shown in Figure 3. During the process, the grinding force generates a large amount of grinding heat when the wheel grinds on the workpiece, and the highest temperature may reach 1450.43 °C. Figure 4 shows the grinding temperature that changes with time at the grinding position in Figure 3. The analysis shows that when the wheel is grinding on this position, the grinding temperature rises rapidly, and the highest temperature of the surface is higher than Ac_3. Meanwhile, the surface microstructure of the 1045 steel workpiece transforms to austenite. Once the grinding wheel leaves this position, considering the heat conductivity of the workpiece itself and the convection heat exchange with the surrounding, the grinding temperature drops rapidly until is lower than Ms, which makes the surface of the workpiece form martensite, thereby achieving the effect of surface strengthening. Figure 5 shows the temperature history for different depth values measured from the free surface of the workpiece. In Figure 5, there is a temperature gradient from the surface to the core. As the depth from the surface increases, the grinding temperature gradually decreases, which is still higher than Ac_1 in a certain depth range. Therefore, hardened layer may generate on the surface.

Table 1. Material parameters of 1045 steel.

Temperature/°C	20	100	200	300	400	500	600	700	800	900	1000
Heat capacity/(J/kg °C)	460	480	498	524	524	615	690	720	682	637	602
Heat conductivity/(W/m °C)	49.77	46.76	43.24	40.29	37.87	35.96	33.18	30.52	27.96	25.92	24.02
Density /(kg/m³)	7850	7830	7800	7770	7740	7700	7685	7672	7660	7651	7649
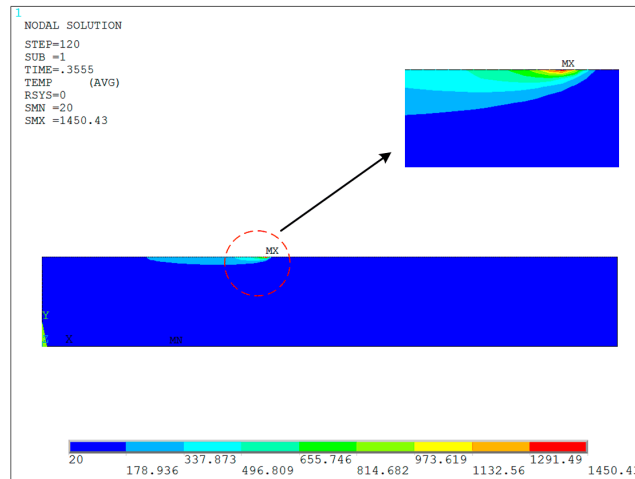
Figure 3. Temperature field in grind-hardening process (a_P = 450 μm, v_w = 10 m/min, v_s = 26.4 m/s).
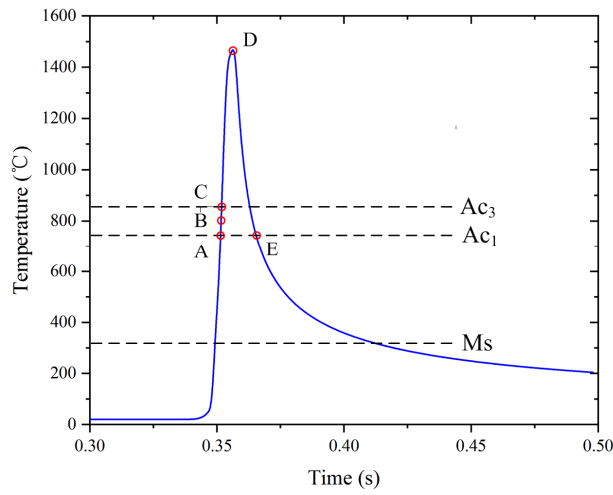
Figure 4. Temperature history with grinding time.
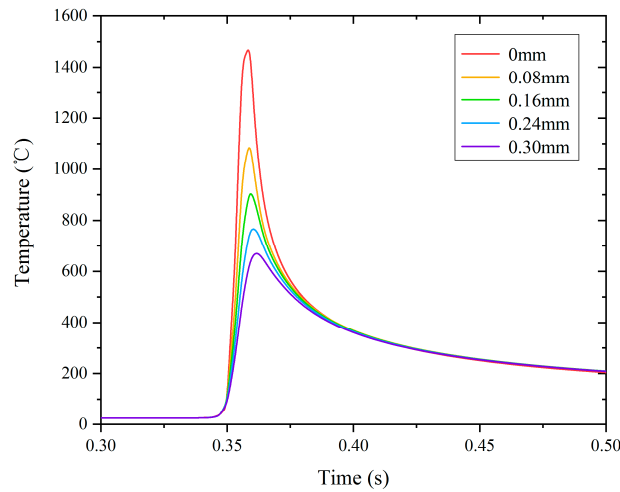
Figure 5. Temperature history for different depth values measured from the free surface.

3.2. Microstructure Transformation Simulation of Hardened Layer

3.2.1. CA Model

Hypoeutectoid-1045 steel is used as the material of the workpiece, whose chemical composition is shown in Table 2. The initial structure of 1045 steel is mainly composed of pearlite and ferrite. Among them, the carbon content of pearlite is 0.77 wt%, and the carbon content of ferrite is 0.01 wt%. The transformation process of the hardened layer is simulated by CA approach, with a 200×200 lattices square domain. Therefore, the entire simulated area is 200×200 lattices with 1 μm for each cell side length L_{CA}. Moore neighbors and a periodic boundary condition are used to simulate an infinite area in the model. Moreover, four state variables are set for each cell, so as to simulate the transformation process of the hardened layer. (1) Crystallographic orientation: different grains are distinguished by crystallographic orientations. All pearlite grains have the same crystallographic orientation which is set to 0. Similarly, all ferrite grains have the same crystallographic orientation which is set to 200. Numbers 1–180 represent orientations of different austenite grains; (2) Cell state: 1 is for pearlite, 2 is for ferrite, 3 is for austenite and 4 is for α/P interface; (3) Color state: cells of pearlite, ferrite and austenite grains with different orientations are distinguished by different colors; (4) Carbon concentration: carbon concentrations at different time are recorded in the cell. The temperature history of each cell in the simulation domain is obtained from the grinding temperature field (as shown in Figure 4). Based on the temperature history of each cell and dynamic model of microstructure transformation, CA simulation is performed on the transformation of the hardened layer.

Table 2. Chemical composition of the 1045 steel.

Element	C	Si	Mn	Cr	Ni	Cu
wt%	0.42–0.5	0.17–0.37	0.5–0.8	0.25	0.3	0.25

#### 3.2.2. Microstructure Transformation Simulation of Hardened Layer

Figure 6 shows the austenitization process of the surface of the workpiece during the grind-hardening process. Cell lattices in different colors represent that grains have different crystallographic orientation. As is shown in Figure 6a, cell lattices that colored in black represents pearlite and colored in white is ferrite. During the process, austenite nucleation begins once the surface temperature reaches Ac_1, namely point A marked in Figure 4, which is shown in Figure 6b. From Figure 6b, the austenite nuclei are formed both in the pearlite and at the α/P interface. Moreover, the number of nucleation at the grain interface is more than that inside the pearlite, which is consistent with the previous theoretical analysis. As grinding temperature grows rapidly (such as B–C in Figure 4), the pearlite will quickly transform into austenite due to the short diffusion distance first. Then the ferrite begins to transform to austenite when 10% of all the pearlite in the simulation area transforms into austenite [29], that is mainly caused by the large carbon concentration gradient between austenite and ferrite at the grain boundary, as shown in Figure 6c. The microstructure distribution of the simulated workpiece when grinding temperature reaches Ac_3 is shown in Figure 6d. The initial microstructure has been transformed into austenite completely with different crystallographic orientations. At this moment, austenite nucleation and growth stop apart from coarsening among austenite grains (corresponding to point C in Figure 4). Figure 6e shows the microstructure distribution of the surface of the workpiece when the grinding temperature reaches the maximum (corresponding to point D in Figure 4). Apparently, as the grinding temperature rises, the austenite grain size gradually increases, while the number of grains continues to decrease. The overall performance is the process of large grains engulfing small ones. Afterwards, the grinding temperature falls as the wheel goes by. The austenite coarsening process does not stop until the grinding temperature falls to Ac_1 (corresponding to point E in Figure 4). It is apparent in Figure 6f that the austenite grain boundaries tend to be flat, and the angle between the grain boundaries is approximately 120°.
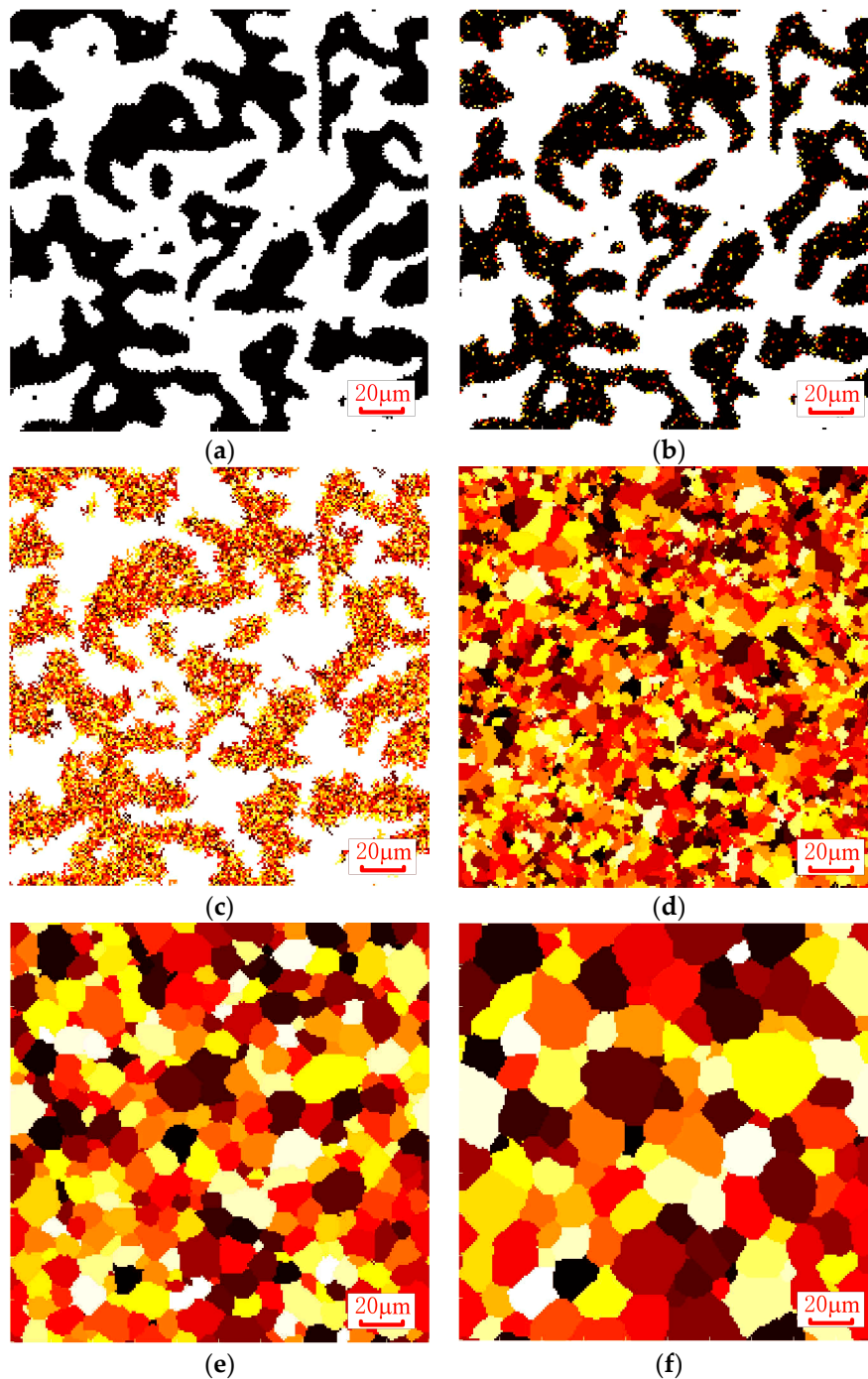
Figure 6. Austenite transformation at different times. (**a**) t = 0 s; (**b**) t = 0.3519 s; (**c**) t = 0.35216 s; (**d**) t = 0.35232 s; (**e**) t = 0.35612 s; (**f**) t = 0.36647 s. (**a**–**c**) white represents ferrite; black represents pearlite; other colors represent austenite grains with different crystallographic orientations; (**d**–**f**) Different colors represent austenite grains with different crystallographic orientations.

When the grinding temperature drops below Ms, martensite transformation begins at the surface of the workpiece. From literature [25,30], lath martensite transformation can be divided into two processes, namely nucleation and grain growth. First of all, the martensite nuclei mainly appear at the austenite boundary. Subsequently, as the temperature falls, martensite grows in 8 directions, whose angle between each growth direction is 45°. Moreover, the martensite grains grow in a certain direction until they contact to other martensite grains in the process of growing. In CA simulation, martensite in different growth directions are indicated with grain orientations 1–8, together with

different colors. Figure 7 shows the transformation process from austenite to martensite in the hardened layer. The initial microstructure distribution of martensite transformation is consistent with the final microstructure distribution of austenite in the hardened layer (Figure 6f), as shown in Figure 7a. The white area represents austenite grains, and the grain boundaries between different austenite grains are distinguished by black lines. The martensite transformation process at different grinding temperatures is illustrated in Figure 7b–d. In accordance with figures, martensite grows rapidly after nucleating at the austenite grain boundaries as the grinding temperature decreases. CA simulation also calculates that the fraction of martensite at different grinding temperatures are 35.6% (280 °C), 78.6% (180 °C), 92.9% (80 °C), respectively.
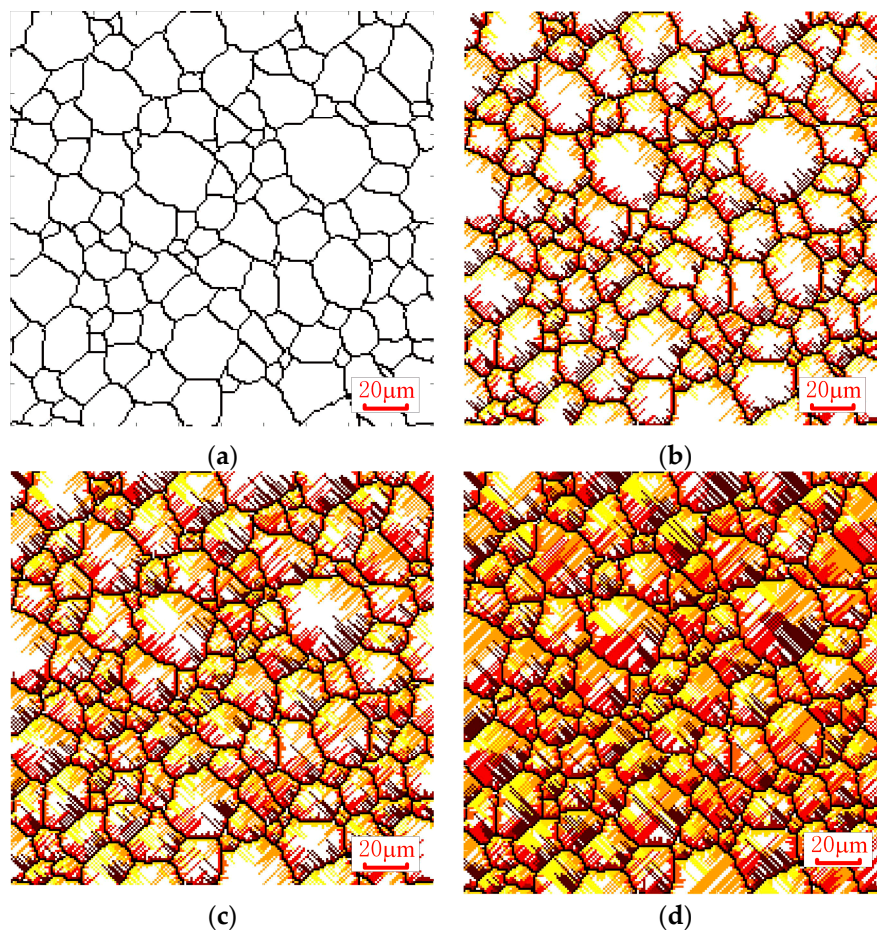
Figure 7. Martensite transformation with different temperatures. (**a**) T = 330 °C; (**b**) T = 280 °C; (**c**) T = 180 °C; (**d**) T= 80 °C.

3.2.3. Prediction of HPD

It can be known from the foregoing that the martensite in the hardened layer is transformed from austenite. Therefore, in HPD prediction, it can be considered that HPD is the distance between the surface of the workpiece and a certain depth that does not appear austenite, where T_{max} is lower than Ac_1. Among others, Ac_1 is given by Equation (5). Moreover, the grinding temperature history is shown in Figure 5. Figure 8 shows the microstructure distribution at different depths (0 mm–0.3 mm) from the surface of the workpiece. It can be figured from Figure 8a–c that the surface microstructure has been completely austenitized since $T_{max} \geq Ac_3$. While the difference in the maximum grinding temperature and heating rate corresponding to the positions along the grinding depth leads to the difference in the number of austenite nuclei and growth velocity. Therefore, there seems different among the grain size and grain number at different positions along the grinding depth. As shown in Figure 8d, if

T_{max} varies in $Ac_1 \leq T_{max} < Ac_3$, the microstructure at this depth is composed of both ferrite and austenite. Since pearlite can quickly transform into austenite when the grinding temperature is within this temperature range. In contrast, the carbon atom at the α/γ interface cannot sufficiently diffuse to the ferrite, which may result in the failure of austenite transformation in workpiece of the ferrite. If $T_{max} < Ac_1$, the microstructure does not transform at this depth, and the microstructure is still composed of ferrite and pearlite, as shown in Figure 8e. Based on the above analysis, HPD with the given parameters is 0.271 mm.
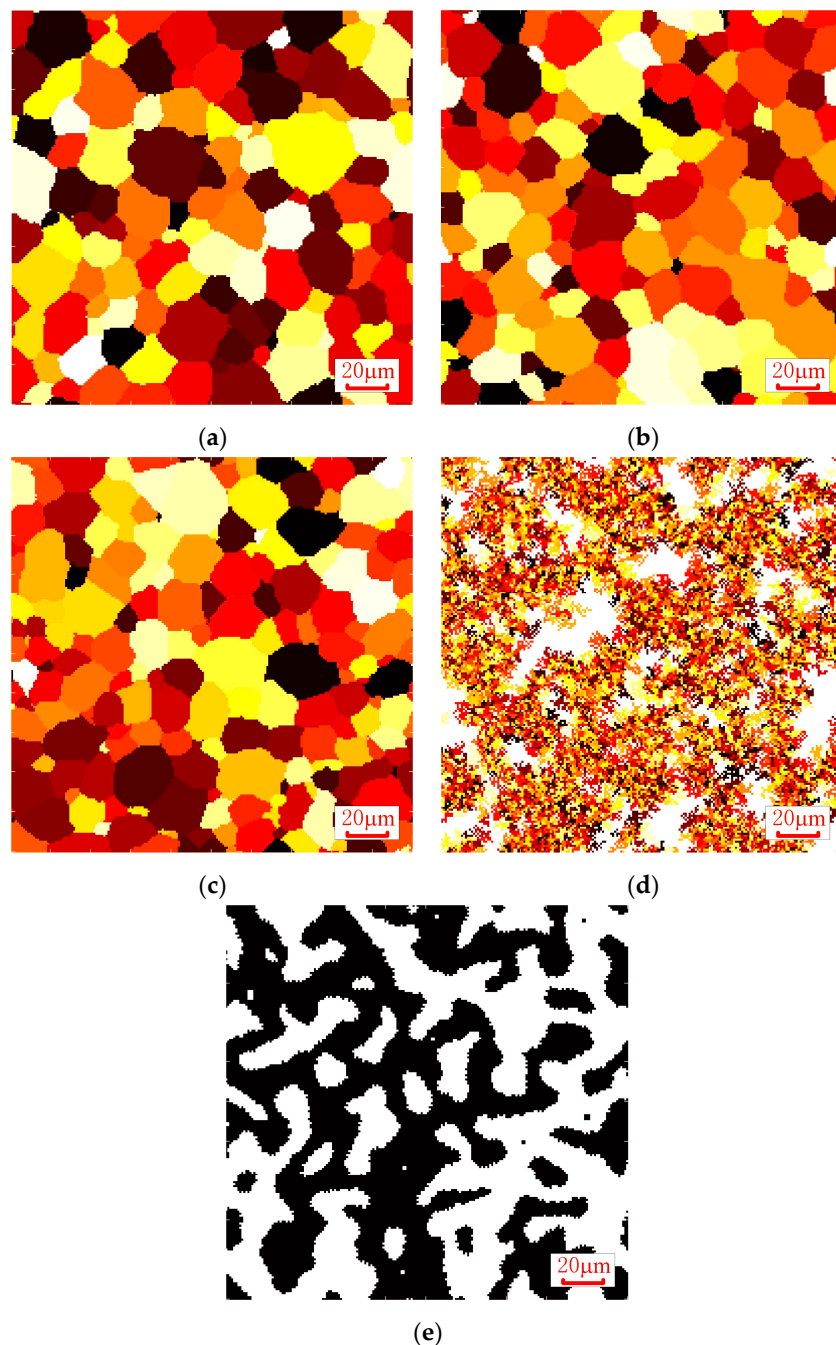
Figure 8. Microstructure distribution at different positions along the grinding depth. (**a**) 0 mm; (**b**) 0.08 mm; (**c**) 0.16 mm; (**d**) 0.24 mm; (**e**) 0.30 mm. (**a**–**c**) Different colors represent austenite grains with different crystallographic orientations; (**d**,**e**) white represents ferrite; black represents pearlite; other colors represent austenite grains with different crystallographic orientations.

HPD prediction with different grinding parameters is shown in Figure 9. Figure also shows that different grinding parameters have a great impact on HPD. The influence law appears that as the a_p and v_w increase, HPD rises accordingly. In addition, a_p has a more significant influence on HPD. This is due to the increase of a_p and v_w improves grinding temperature that results in an increase in HPD.
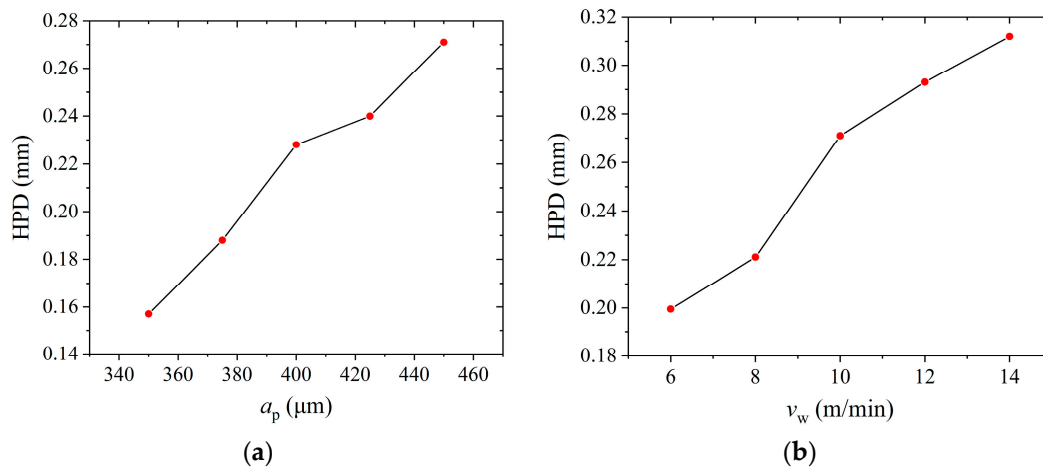
Figure 9. HPD prediction with different grinding parameters. (**a**) $v_w = 10$ m/min, $v_s = 26.4$ m/s; (**b**) $a_p = 450$ μm, $v_s = 26.4$ m/s.

4. Experimental Validation of the Analysis

The grind-hardening experiment is carried out on the ORBIT36CNC surface grinder (Korber Schleifring, Shanghai, China). A white alumina wheel, with the diameter 350 mm and width 40 mm, respectively, is used in the experiment. Moreover, the granularity of the wheel is F46. The material of the experimental workpiece is non-quenching 1045 steel, with the size 90 mm × 9 mm × 14 mm. The grinding modes is down grinding. In order to obtain a large amount of grinding heat on the surface of the workpiece, the cooling liquid is not involved in the experiment. Parameters in grind-hardening experiment are listed in Table 3.

**Table 3.** Parameters in grind-hardening experiment.

No.	a_p (μm)	v_w (m/min)	v_s (m/s)
1	350	10	
2	375	10	
3	400	10	
4	425	10	
5	450	10	26.4
6	450	6	
7	450	8	
8	450	12	
9	450	14	

Surface microstructure of the workpiece before and after grinding are observed by S-400 metallurgical microscope. Figure 10 clearly shows that the initial structure before the grind-hardening experiment is composed of both pearlite and ferrite. It can be seen from Figure 11 that the surface microstructure has transformed after grinding that forming HPD dominated by martensite. Based on the microstructure distribution characteristics, the hardened layer can be divided into fully hardened layer and transition hardened layer. Among them, the fully hardened layer is mainly composed of lath martensite and retained austenite, whereas the transition one is composed of martensite and ferrite. The measurement has found that HPD is 0.259 mm with grinding parameters $a_p = 450$ μm,

v_w = 10 m/min and v_s = 26.4 m/s. Matrix remains below the transition hardened layer, which is still composed of ferrite and pearlite, which is much more fragmented than the initial microstructure.
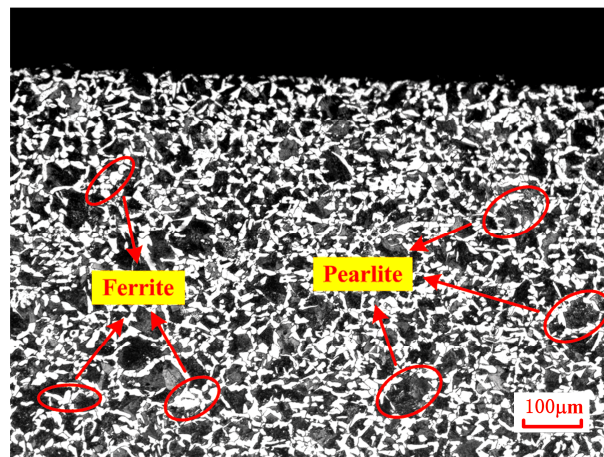
Figure 10. Initial microstructure before grind-hardening experiment by metallurgical microscopy.
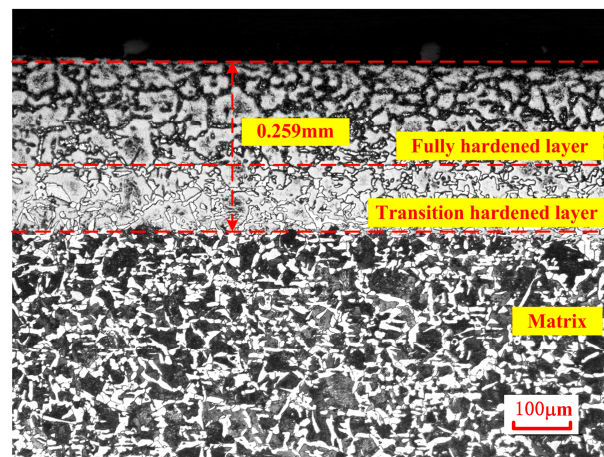
Figure 11. Microstructure after grind-hardening experiment by metallurgical microscopy.

From the comparison between the predicted value of HPD and the experimental value with different grinding parameters (as shown in Table 4), the trend of the experimental value is consistent with the theoretical analysis. In addition, from the comparison, there is a small difference between the predicted value and the experimental value. On the basis of the above study, it is convinced that the CA method proposed in this paper is an effective approach for HPD prediction.

Table 4. Comparison between the predicted value and the experimental value of hardness penetration depth (HPD).

No.	a_p (μm)	v_w (m/min)	v_s (m/s)	Predicted Value (mm)	Experimental Value (mm)	Difference (%)
1	350	10		0.157	0.169	7.1%
2	375	10		0.188	0.201	6.47%
3	400	10		0.228	0.246	7.31%
4	425	10		0.240	0.247	2.83%
5	450	10	26.4	0.271	0.259	4.63%
6	450	6		0.204	0.219	6.85%
7	450	8		0.221	0.232	4.74%
8	450	12		0.283	0.274	3.28%
9	450	14		0.312	0.296	5.4%

5. Conclusions

To sum up, studies on the temperature field distribution of the hypoeutectoid-1045 steel surface of the workpiece in grind-hardening process were carried out and the evolution of the microstructure was dynamically simulated for revealing the formation mechanism of the hardened layer and predicting its depth. Further, the simulation results were effectively verified by grind-hardening experiments. The conclusions of the study are summarized as follows:

(1) The instantaneous change and distribution of the temperature field of the surface of the workpiece were studied during grind-hardening process by FEM. The study found that the maximum grinding temperature of the surface of the workpiece is higher than Ac_1, which can reach 1450.43 °C, and the minimum temperature is lower than Ms, with grinding parameters a_p = 450 μm, v_w = 10 m/min and v_s = 26.4 m/s;

(2) The microstructure transformation process of the hardened layer was dynamically simulated based on CA approach. Simulation result displayed that initial microstructure transformed to austenite gradually, whose process included austenite nucleation, growth and coarsening as soon as the grinding temperature was higher than Ac_1. When the grinding temperature dropped lower than Ms, the austenite transformed to martensite. Moreover, the fraction of martensite gradually increased as the grinding temperature dropped;

(3) During the grind-hardening process, the microstructure distribution at different positions along grinding depth was simulated as well. For the positions, whose grinding temperatures were above Ac_3, the microstructure merely consisted of austenite. In contrast, the microstructure at a certain position in the workpiece was composed of both austenite and ferrite, whose maximum grinding temperature varied from Ac_1 to Ac_3. Further studies were carried out on HPD prediction with different grinding parameters. Moreover, grind-hardening experiments was carried out to assess the validity of the HPD prediction model. Comparison between experimental value and the predicted value found that the difference, varied in 2.83%–7.31%, was tiny that HPD prediction model is verified to be effective.

(4) HPD showed a growing trend as a_p and v_w rises. Among them, a_p had a more significant influence on HPD.

References

1. Brinksmeier, E.; Brockhoff, T. Utilization of grinding heat as a new heat treatment process. *CIRP Ann. Manuf. Technol.* **1996**, *45*, 283–286. [CrossRef]
2. Deng, Y.S.; Xiu, S.C.; Shi, X.L.; Sun, C.; Wang, Y.S. Study on the effect mechanisms of pre-stress on residual stress and surface roughness in PSHG. *Int. J. Adv. Manuf. Technol.* **2017**, *88*, 3243–3256. [CrossRef]
3. Nguyen, T.; Zhang, L.C.; Sun, D.L.; Wu, Q. Characterizing the mechanical properties of the hardened layer induced by grinding-hardening. *Mach. Sci. Technol.* **2014**, *18*, 277–298. [CrossRef]
4. Brinksmeier, E.; Brockhoff, T. Surface heat treatment by using advanced grinding processes. *Metall. Ital.* **1999**, *91*, 19–23.
5. Brockhoff, T. Grind-hardening: A comprehensive view. *CIRP Ann. Manuf. Technol.* **1999**, *48*, 255–260. [CrossRef]

6.   Foeckerer, T.; Zaeh, M.F.; Zhang, O.B. A three-dimensional analytical model to predict the thermo-metallurgical effects within the surface layer during grinding and grind-hardening. *Int. J. Heat Mass Transf.* **2013**, *56*, 223–237. [CrossRef]

7.   Alonso, U.; Ortega, N.; Sanchez, J.A.; Pombo, I.; Izquierdo, B.; Plaza, S. Hardness control of grind-hardening and finishing grinding by means of area-based specific energy. *Int. J. Mach. Tools Manuf.* **2015**, *88*, 24–33. [CrossRef]

8.   Liu, S.Y.; Yang, G.; Zheng, J.Q.; Liu, X.H. Numerical and experimental studies on grind-hardening cylindrical surface. *Int. J. Adv. Manuf. Technol.* **2015**, *76*, 487–499. [CrossRef]

9.   Huang, X.M.; Ren, Y.H.; Wu, W.; Li, T. Research on grind-hardening layer and residual stresses based on variable grinding forces. *Int. J. Adv. Manuf. Technol.* **2019**, *103*, 1045–1055. [CrossRef]

10. Zhao, Y.; Chen, D.F.; Long, M.J.; Arif, T.T.; Qin, R.S. A Three-Dimensional Cellular Automata Model for Dendrite Growth with Various Crystallographic Orientations During Solidification. *Metall. Mater. Trans. B* **2014**, *45*, 719–725. [CrossRef]

11. Sieradzki, L.; Made, L. A perceptive comparison of the cellular automata and Monte Carlo techniques in application to static recrystallization modeling in polycrystalline materials. *Comput. Mater. Sci.* **2013**, *67*, 156–173. [CrossRef]

12. Salehi, M.S.; Serajzadeh, S. Simulation of static recrystallization in non-isothermal annealing using a coupled cellular automata and finite element model. *Comput. Mater. Sci.* **2012**, *53*, 145–152. [CrossRef]

13. Monshat, H.; Serajzadeh, S. Simulation of austenite decomposition in continuous cooling conditions: A cellular automata-finite element modeling. *Ironmak. Steelmak.* **2019**, *46*, 513–521. [CrossRef]

14. Yang, B.J.; Chuzhoy, L.; Johson, M.L. Modeling reaustenitization of hypoeutectoid steels with cellular automaton method. *Comput. Mater. Sci.* **2007**, *41*, 186–194. [CrossRef]

15. An, D.; Pan, S.Y.; Hang, L.; Dai, T.; Krakauer, B.; Zhu, M.F. Modeling of Ferrite-Austenite Phase Transformation Using a Cellular Automaton Model. *ISIJ Int.* **2014**, *54*, 422–429. [CrossRef]

16. Halder, C.; Bachniak, D.; Madej, L.; Chakraborti, N.; Pietrzyk, M. Sensitivity Analysis of the Finite Difference 2-D Cellular Automata Model for Phase Transformation during Heating. *ISIJ Int.* **2015**, *55*, 285–292. [CrossRef]

17. Su, F.Y.; Liu, W.L.; Wen, Z. Three-dimensional cellular automaton simulation of austenite grain growth of Fe-1C-1.5Cr alloy steel. *J. Mater. Res. Technol.* **2020**, *9*, 180–187. [CrossRef]

18. Yu, X.X.; Lau, W.S. A finite-element analysis of residual stress in stretch grinding. *J. Mater. Process Technol.* **1999**, *94*, 13–22. [CrossRef]

19. Guo, Y.; Xiu, S.C.; Liu, M.H.; Shi, X.L. Uniformity mechanism investigation of hardness penetration depth during grind-hardening process. *Int. J. Adv. Manuf. Technol.* **2017**, *89*, 2001–2010. [CrossRef]

20. Yang, B.J.; Hattiangadi, A.; Li, W.Z.; Zhou, G.F.; McGreevy, T.E. Simulation of steel microstructure evolution during induction heating. *Mater. Sci. Eng. A* **2010**, *527*, 2978–2984. [CrossRef]

21. Sun, C.; Duan, J.C.; Lan, D.X.; Liu, Z.X.; Xiu, S.C. Prediction about ground hardening layers distribution on grinding chatter by contact stiffness. *Arch. Civ. Mech. Eng.* **2018**, *18*, 1626–1642. [CrossRef]

22. Zhu, B.; Zhang, Y.S.; Wang, C.; Liu, P.X.; Liang, W.K.; Li, J. Modeling of the Austenitization of Ultra-high Strength Steel with Cellular Automation Method. *Metall. Mater. Trans. A* **2014**, *45A*, 3161–3171. [CrossRef]

23. Su, B.; Han, Z.Q.; Liu, B.C. Cellular Automaton Modeling of Austenite Nucleation and Growth in Hypoeutectoid Steel during Heating Process. *ISIJ Int.* **2013**, *53*, 527–534. [CrossRef]

24. Halder, C.; Madej, L.; Pietrzyk, M. Discrete micro-scale cellular automata model for modeling phase transformation during heating of dual phase steels. *Arch. Civ. Mech. Eng.* **2014**, *14*, 96–103. [CrossRef]

25. Sun, C.; Liu, Z.X.; Lan, D.X.; Duan, J.C.; Xiu, S.C. Study on the influence of the grinding chatter on the workpiece's microstructure transformation. *Int. J. Adv. Manuf. Technol.* **2018**, *96*, 3861–3879. [CrossRef]

26. Zheng, C.W.; Xiao, N.M.; Li, D.Z.; Li, Y.Y. Microstructure prediction of the austenite recrystallization during multi-pass steel strip hot rolling: A cellular automaton modeling. *Comput. Mater. Sci.* **2008**, *44*, 507–514. [CrossRef]

27. Andrews, K.W. Empirical formulae for calculation of some transformation temperatures. *J. Iron Steel Inst.* **1965**, *203*, 721–727.

28. Liu, M.H.; Zhang, K.; Xiu, S.C. Mechanism investigation of hardening layer hardness uniformity based on grind-hardening process. *Int. J. Adv. Manuf. Technol.* **2017**, *88*, 3185–3194. [CrossRef]

29. Deng, Y.S.; Xiu, S.C. Research on microstructure evolution of austenitization in grinding hardening by cellular automata simulation and experiment. *Int. Adv. Manuf. Technol.* **2017**, *93*, 2599–2612. [CrossRef]

30. Zhi, Y.; Liu, W.J.; Liu, X.H. Simulation of Martensitic Transformation of High Strength and Elongation Steel by Cellular Automaton. *Adv. Mat. Res.* **2014**, *1004–1005*, 235–238. [CrossRef]